Volume 22
Number 14
15 April 2026
Pages 2589–2772

Soft Matter

rsc.li/soft-matter-journal

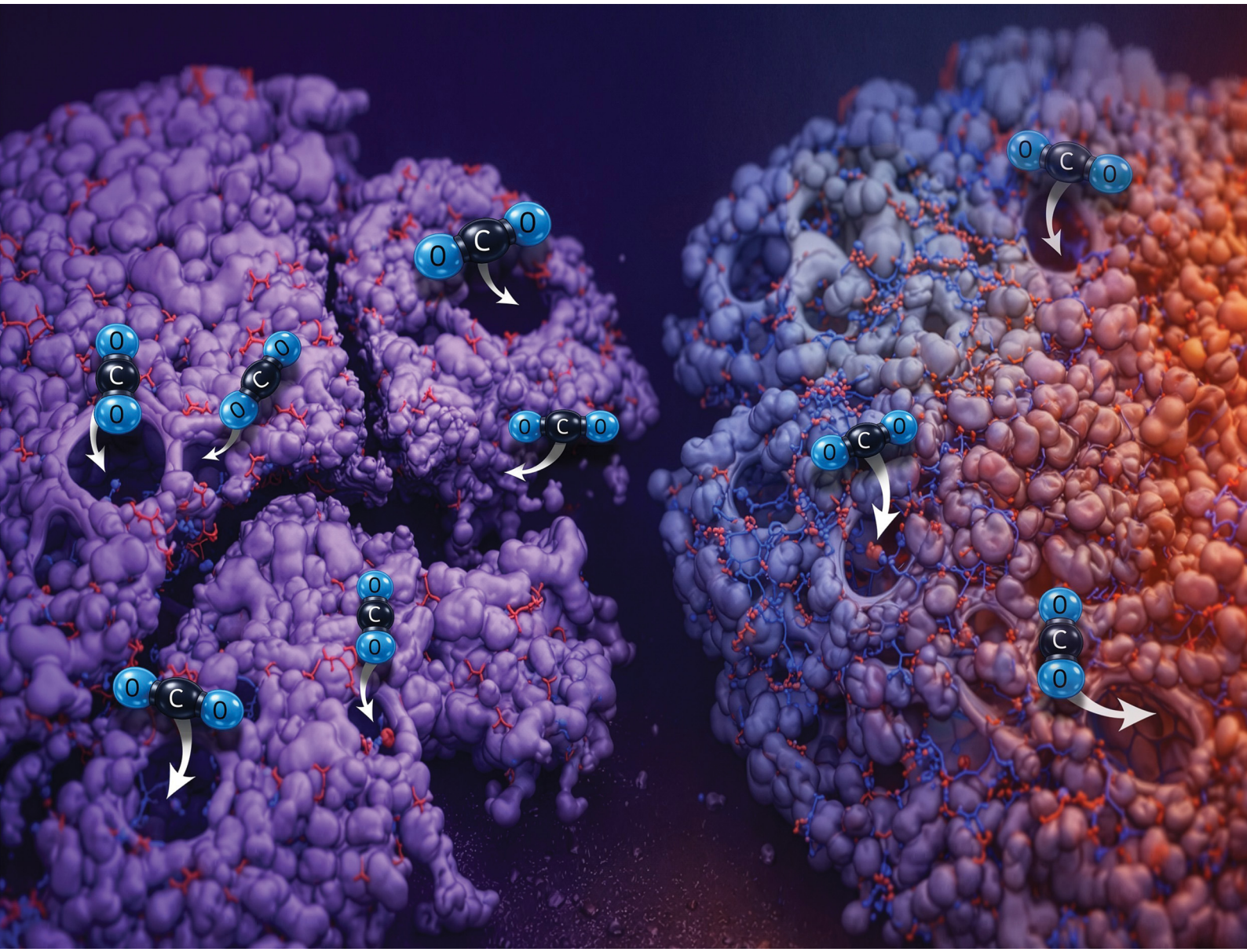

ISSN 1744-6848

ROYAL SOCIETY OF CHEMISTRY

PAPER

Jason E. Bara, Jihong A. Ma *et al.*

Ionic-content-driven restructuring of spirobisindane ionene networks: implications for mechanics, self-healing, and gas transport

Soft Matter

PAPER

View Article Online
View Journal | View Issue

Check for updates

Cite this: *Soft Matter*, 2026, 22, 2608

Ionic-content-driven restructuring of spirobisindane ionene networks: implications for mechanics, self-healing, and gas transport

Fatemeh Sabokroozroozbahani, [a] Sudhir Ravula, [b] Alain Tundidor Camba, [b] Pravin S. Shinde, [b] Jong Keum, [cd] Jason E. Bara *[b] and Jihong A. Ma *[aef]

Polymers of intrinsic microporosity (PIMs) offer exceptional gas permeability but remain brittle and susceptible to physical aging, limiting their durability in separation applications. Here, we introduce a reconfigurable microporous polymer network that uniquely integrates permanent PIM microporosity with autonomous, intrinsic self-healing driven by imidazolium-based ionic motifs. Spirobisindane units generate the intrinsic free-volume architecture, while an imidazolium-containing polyamide ionene supplies dynamic ionic and hydrogen-bonding interactions that reorganize under mild activation. Incorporation of imidazolium-based ionic liquids further tunes cohesion, mobility, and densification, enabling the network to relax, re-associate, and retain microporosity without structural collapse. Through a comprehensive multiscale approach combining spectroscopy, scattering, thermal and mechanical characterization with all-atom molecular dynamics and density functional theory calculations, we elucidate how ionic content, as a single control parameter that reshapes free-volume distributions, modulates local coordination environments, and governs relaxation and healing kinetics. At intermediate ionic loadings, the networks achieve rapid, repeatable self-healing while maintaining CO_2 selectivity, demonstrating an optimal balance between segmental mobility and structural integrity. By establishing how hierarchical ionic interactions couple structure, dynamics, and transport in microporous ionene networks, this work provides generalizable design rules for adaptive soft-matter systems that require simultaneous mechanical resilience, reconfigurability, and selective gas transport.

Received 4th February 2026,
Accepted 2nd March 2026

DOI: 10.1039/d6sm00105j

rsc.li/soft-matter-journal

Open Access Article. Published on 04 March 2026. Downloaded on 5/11/2026 10:44:53 PM.
This article is licensed under a Creative Commons Attribution-NonCommercial 3.0 Unported Licence.

1. Introduction

The rise of atmospheric carbon dioxide (CO_2) driven by fossil fuel consumption and land-use change continues to intensify global climate risks,[1] motivating the development of efficient and low-energy separation technologies for carbon capture. Polymeric gas-separation membranes are attractive candidates due to low energy demand, minimal maintenance, and modular operation.[2] Their performance is governed by the solution-diffusion mechanism, in which gas permeability

$$P_i = D_i K_{si} \quad (1)$$

reflects the product of diffusivity D_i and solubility K_{si}, while selectivity (eqn (2))

$$\alpha_{i/j} = \frac{P_i}{P_j} = \frac{D_i}{D_j}\frac{K_{si}}{K_{sj}} \quad (2)$$

quantifies discrimination between gas species i and j. In most polymers, increasing free volume enhances diffusion (and thus permeability) but compromises selectivity, giving rise to the well-known Robeson upper bound.[3,4]

Polymers of intrinsic microporosity (PIMs) partially overcome this trade-off. Their rigid, contorted backbones generate interconnected sub-2 nm pores that facilitate rapid gas transport, while aromatic and polar functional groups can enhance CO_2 interactions.[5–9] These attributes often enable performance beyond the Robeson upper bound. However, the same microporosity that underpins exceptional permeability also often renders PIMs mechanically fragile and susceptible to physical aging,[10] leading to diminished long-term durability and reduced separation efficiency.[11] Strategies that extend membrane lifetime, reliability, and sustainability – by introducing mechanical compliance without sacrificing stiffness, and

[a] *Department of Mechanical Engineering, University of Vermont, Burlington, Vermont 05405, USA. E-mail: Jihong.Ma@uvm.edu*
[b] *Department of Chemical & Biological Engineering, University of Alabama, Tuscaloosa, Alabama 35487, USA. E-mail: jbara@eng.ua.edu*
[c] *Center for Nanophase Materials and Sciences, Oak Ridge National Laboratory, Oak Ridge, Tennessee 37830, USA*
[d] *Neutron Scattering Division, Oak Ridge National Laboratory, Oak Ridge, Tennessee 37830, USA*
[e] *Department of Physics, University of Vermont, Burlington, Vermont 05405, USA*
[f] *Materials Science Program, University of Vermont, Burlington, Vermont 05405, USA*

This journal is © The Royal Society of Chemistry 2026

Open Access Article. Published on 04 March 2026. Downloaded on 5/11/2026 10:44:53 PM.
This article is licensed under a Creative Commons Attribution-NonCommercial 3.0 Unported Licence.

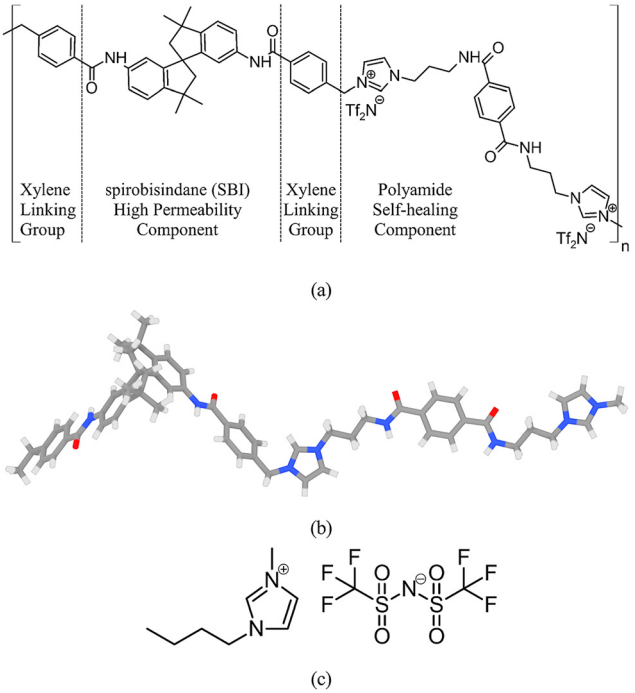

Fig. 1 Structural illustrations of the polymer system: (a) schematic of the SBI-TC-API-PA1 monomer with the SBI segment, self-healing segment, and linking groups; (b) corresponding relaxed molecular configuration of the polymer chain; (c) molecular structure of the ionic liquid, shown as the $[C_4mim]^+/[Tf_2N]^-$ ion pair.

ideally incorporating self-healing (SH) mechanisms – are, therefore, highly desirable, particularly for demanding environments where mechanical damage and wear are unavoidable.

Intrinsically self-healing polymers (ISHPs) offer a compelling route toward mechanically resilient membranes.[12–17] While extrinsic approaches such as capsule- or vascular-based healing can repair damage,[18] they are typically irreversible and undesirable for long-term use. By contrast, intrinsic strategies, such as Diels–Alder (DA) chemistry,[19] H-bonding,[20–23] electrostatic interactions in ionic liquids (ILs) or poly(IL) copolymers,[24–28] and ionene-based associative networks,[29–31] enable repeatable healing, often under mild conditions, and are particularly attractive for carbon-capture membranes.[9,19] Among these, imidazolium-based motifs stand out due to their strong yet dynamic ionic and H-bonding interactions, charge-mediated segmental mobility, and chemical tunability through counterion selection.[32] Importantly, integrating imidazolium groups into polyamides – otherwise dominated by dense, crystalline amide H-bond networks with limited chain mobility at ambient temperature – can disrupt crystallinity, increase polymer mobility, and introduce reversible ionic-amide crosslinks that can reconfigure and re-associate near room temperature.[29,30]

Despite the promise of ionic self-healing architectures, it remains unclear how integrating imidazolium-based, ISHP polyamide (PA) ionenes with PIM architectures affects the coupled structure–dynamics–transport relationships that govern both gas separation and self-healing performance. Specifically, the field lacks a mechanistic understanding of how ionic content orchestrates changes in micropore connectivity, local coordination environment, segmental mobility, and nonequilibrium healing pathways – factors that together determine mechanical resilience and selective gas transport. Addressing this gap requires a holistic, multiscale approach capable of connecting molecular interactions to mesoscale free-volume reorganization and macroscopic function.

In this work, we introduce a reconfigurable microporous polymer network that unites permanent PIM microporosity with autonomous, imidazolium-driven intrinsic self-healing. Our architecture couples (i) spirobisindane (SBI) units, whose contorted geometry yields the interconnected voids responsible for the intrinsic microporosity of PIMs, with (ii) an imidazolium-containing PA-ionene (TC-API-PA1) that imparts self-healing *via* reversible H-bonding and ionic interactions[32,33] (Fig. 1(a) and (b)). The network's ionic content is further modulated using bis(trifluoromethanesulfonyl)imide ($[Tf_2N]^-$) counterions and an imidazolium-based IL, 1-butyl-3-methylimidazolium bis(trifluoromethanesulfonyl)imide ($[C_4mim][Tf_2N]$, Fig. 1(c)), enabling ionic content to function as a single control parameter governing densification, segmental mobility, and selective transport. Although ILs may exhibit plasticization behavior,[34] they differ fundamentally from neutral small-molecule plasticizers: in addition to dilution effects, they participate in specific coordination interactions and form ionic aggregates that reorganize polymer packing and dynamics.[35,36] Consistent with ionically associated polymer networks, such ionic clustering can act as reversible physical crosslinks, producing coupled changes in mobility and cohesion.[30] Accordingly, throughout this work, we treat 'ionic content' as a practical formulation knob, with the observed restructuring attributed to ionic coordination and clustering rather than dilution alone.

Through an integrated experimental-computational approach combining advanced polymer synthesis, spectroscopy, scattering, thermal and mechanical measurements, all-atom molecular dynamics (MD) simulations, and density-functional theory (DFT) calculations, we uncover how ionic interactions reorganize the free-volume landscape, modulate local coordination, and regulate nonequilibrium relaxation during healing. We show that intermediate ionic loading yields an optimal balance between mobility and cohesion, enabling rapid self-healing while preserving CO_2 selectivity. By establishing how hierarchical ionic interactions couple structure, dynamics, and transport, this work provides generalized design principles for adaptive soft-matter systems that require durable mechanics, reconfigurability, and selective gas transport.

2. Results and discussion

2.1. Polymer synthesis and structural characterization

Understanding how ionic content reshapes the internal landscape of SBI-based ionene networks requires a coordinated examination of polymer architecture across multiple length scales. In this section, we establish the structural foundations

Open Access Article. Published on 04 March 2026. Downloaded on 5/11/2026 10:44:53 PM.
This article is licensed under a Creative Commons Attribution-NonCommercial 3.0 Unported Licence.

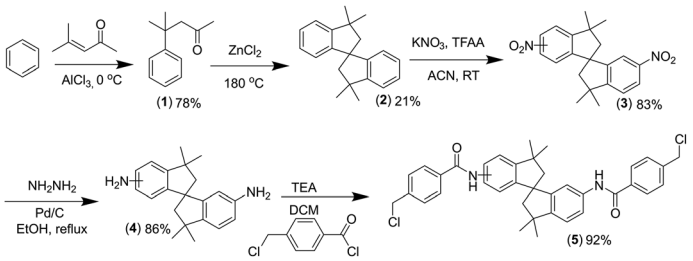

Scheme 1 Synthetic route for the obtention of the dihalogenated monomer **5**.

on which all subsequent thermomechanical, healing, and transport behavior emerge. We begin by outlining the synthesis and film-formation procedures that produce well-defined, composition-controlled materials. We then probe how IL incorporation reorganizes chain packing, microporosity, and local coordination environments using X-ray scattering and all-atom molecular simulations. Together, these analyses reveal how ionic interactions modulate both conformational flexibility and free-volume organization – providing the structural basis for the dynamic responses explored in later sections.

2.1.1. Polymer synthesis and film preparation. To interrogate how ionic content governs structure, dynamics, and transport in reconfigurable microporous networks, we first synthesized the SBI-based PA-ionene (SBI-TC-API-PA1) and prepared dense polymer films suitable for multiscale characterization. The synthetic route (Schemes 1 and 2) follows a stepwise strategy designed to integrate rigid SBI segments, which generate intrinsic microporosity, with imidazolium-containing PA-ionene linkages that impart dynamic, reversible ionic interactions.

The dihalogenated SBI monomer **5** was obtained through a multi-step sequence beginning with diamine **4**, prepared as an isomeric mixture *via* a route adapted from Carta *et al.*,[37] (Scheme 1). Subsequent functionalization of diamine **4** with 4-(chloromethyl)benzoyl chloride introduced the requisite benzylic halide functionality, affording the dihalogenated monomer **5** and completing the overall five-step synthesis with a total yield of 11%. Full synthetic details are provided in Methodology – Synthesis of the dihalogenated monomer.

The imidazolium-containing ionene SBI-TC-API-PA1 was then synthesized by a Menshutkin (S_N2) polymerization between the dihalide **5** and the di-imidazole monomer TC-API (Scheme 2). Following polymerization, the crude material was purified through sequential solvent washing and subsequently subjected to anion exchange with $LiTf_2N$ to afford the imidazolium-based ionene bearing $[Tf_2N]^-$ counterions. Full experimental procedures are described in Methodology – Synthesis of polymer SBI-TC-API-PA1.

After purification, dense polymer films were fabricated by solution casting from DMF, followed by controlled solvent evaporation and thermal annealing to promote uniform network formation. The resulting membranes were optically clear, mechanically robust, and free of visible defects, providing well-defined samples for structural, thermomechanical, and transport measurements. For composite systems, the IL $[C_4mim][Tf_2N]$ was incorporated directly into the polymer solution at prescribed loadings relative to the polymer repeat unit. Increasing IL content produces progressively smoother and more homogeneous film surfaces (Fig. 2), consistent with enhanced chain relaxation and reduced interchain friction during film formation. This approach yields homogeneous films with reproducible ionic content and ensures that IL molecules are intimately integrated within the network rather than phase separated at interfaces. Full film-casting procedures are provided in Methodology – Film preparation.

By establishing reliable synthesis and film preparation protocols, we created a controlled platform in which ionic content can be varied systematically. This foundation enables the analyses that follow, where we examine how IL incorporation restructures polymer organization and governs the macroscopic behavior of these adaptive microporous networks.

2.1.2. Matrix densification and conformational stability. With the polymer successfully synthesized and processed into uniform films, we next examined how IL incorporation alters chain organization and free-volume architecture in the solid state. These structural responses are central to both mechanical and transport behavior, as ionene membranes derive their

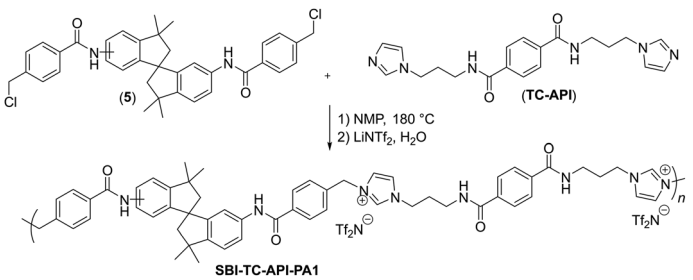

Scheme 2 Synthetic route for the obtention of the ionene SBI-TC-API-PA1.

Open Access Article. Published on 04 March 2026. Downloaded on 5/11/2026 10:44:53 PM.
This article is licensed under a Creative Commons Attribution-NonCommercial 3.0 Unported Licence.

Fig. 2 Photographs of (a) neat ionene films and films containing (b) 0.5, (c) 0.75, (d) 1.0 and (e) 1.25 equivalents (eq) of the ionic liquid (IL) [C_4mim][Tf_2N] per monomer. Increasing IL loading (c–e) leads to progressively smoother and more homogeneous films, indicative of IL-facilitated chain relaxation and enhanced film formation.

function from the interplay between chain packing, microporosity, and segmental mobility. To resolve these effects across multiple lengthscales, we combined wide- and small-angle X-ray diffraction (WAXS/SAXS) with all-atom MD simulations.

WAXS patterns (Fig. 3b) indicate that both the neat polymer and IL-containing composites remain amorphous, as evidenced by the absence of sharp diffraction peaks. Notably, the position of the broad scattering maximum remains essentially unchanged upon IL incorporation, corresponding to an average interchain spacing of approximately 4.47 Å. This invariance suggests that the dominant short-range packing motif – arising from the balance between rigid aromatic segments and flexible spacers – is preserved. The ability of the backbone to accommodate IL molecules through local rearrangements likely renders WAXS insensitive to more subtle reorganizations of free volume.

To probe mesoscale structural changes beyond nearest-neighbor packing, SAXS measurements were performed. The neat polymer exhibits a pronounced correlation peak near 0.2 $Å^{-1}$ (Fig. 3b), characteristic of the intrinsic microporous network generated by the SBI-based motif, corresponding to an average pore–pore correlation distance of approximately 31.4 Å. Upon IL incorporation, this signature is significantly broadened and diminished in intensity, indicating a loss of well-defined nanostructural periodicity. This observation suggests that ILs act as active penetrants that disrupt the intrinsic free-volume network rather than occupying isolated interfacial regions.

While SAXS provides clear evidence of microporous disruption, scattering alone cannot distinguish pore filling from large-scale chain rearrangement. To resolve this ambiguity, we performed all-atom MD simulations of systems containing either four (4-mer) or eight (8-mer) repeat units per chain across a range of IL concentrations. Following rigorous equilibration, the fractional free volume (FFV) was quantified using an α-shape construction with a 2.7 Å probe radius, representative of gas-accessible micropores.

As shown in Fig. 4c, FFV decreases monotonically with increasing IL content and is largely independent of chain length. This trend confirms that IL molecules progressively infiltrate and occupy intrinsic microporous regions rather than inducing backbone collapse. Consistent with this interpretation, the overall system density increases with IL loading (Fig. 4d), reflecting matrix densification driven by pore filling. In gas-separation membranes, such densification would typically enhance selectivity at the cost of permeability.[38]

To assess whether IL incorporation also alters chain conformation, we evaluated the radius of gyration, R_g, as a function of IL content. For shorter chains (4-mers), R_g remains nearly constant, reflecting their inherent rigidity. In contrast, 8-mer chains exhibit a clear increase in R_g with increasing IL concentration (Fig. 5, indicating IL-induced chain extension. Analysis using the scaling law $R_g \propto N^{\nu}$ (where N represents the number of monomers per chain) shows that the Flory exponent ν increases from $\sim$1/3 in the neat polymer – consistent with collapsed polymer configurations – to 0.585 at an IL concentration of n = 2.0, indicative of more extended chains.

Importantly, this conformational relaxation does not translate into increased free volume. Instead, the combined SAXS

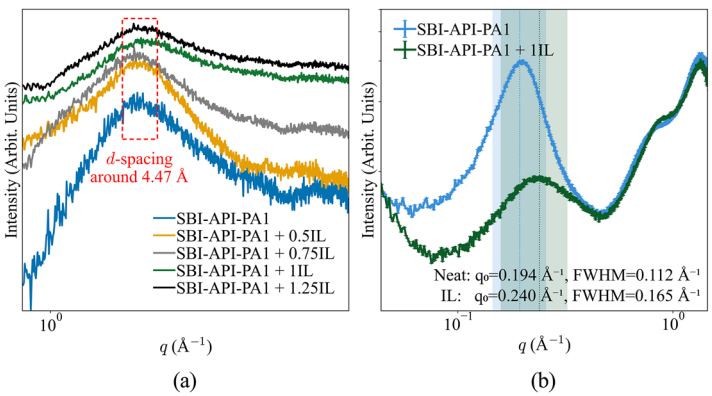

Fig. 3 Structural characterization of ionene/IL composites. (a) WAXS diffractograms of ionenes with varying IL concentrations. (b) SAXS profiles of neat SBI-TC-API-PA1 and the 1.0 eq IL composite. Error bars represent instrumental uncertainty.

Open Access Article. Published on 04 March 2026. Downloaded on 5/11/2026 10:44:53 PM.
This article is licensed under a Creative Commons Attribution-NonCommercial 3.0 Unported Licence.

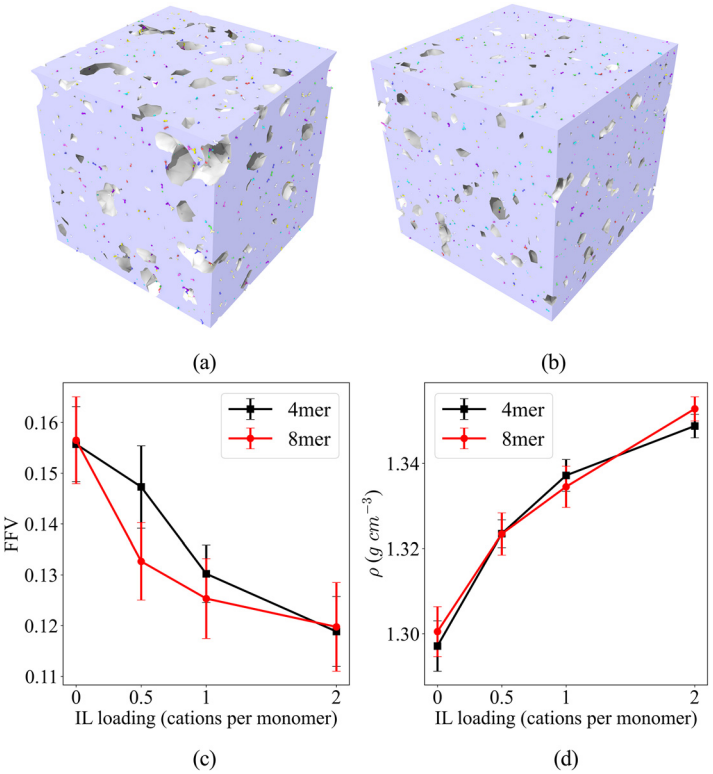

Fig. 4 Equilibrated polymer systems showing reduced void spaces with increasing IL concentration: (a) 8-mer without cations; (b) 8-mer with 2 cations per monomer; (c) FFV and (d) density as a function of cation concentration (error bars represent standard deviations (SD) across independent trajectories).

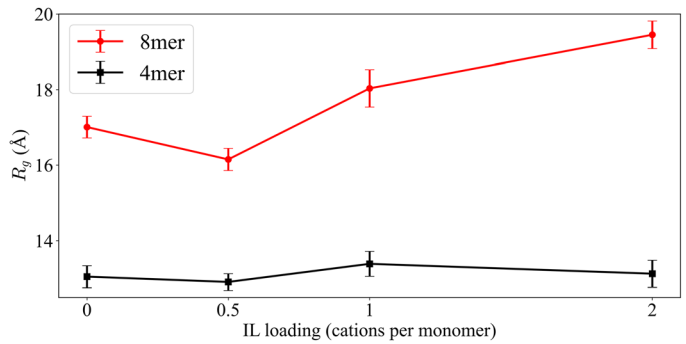

Fig. 5 R_g of 4-mer and 8-mer polymers *vs.* cation concentration; error bars represent SD from independent simulations.

and FFV results demonstrate that IL molecules dominate the free-volume landscape by filling intrinsic micropores, such that the net effect is densification rather than expansion.

Together, these results establish a coherent multiscale picture: IL incorporation preserves short-range chain packing, promotes modest chain extension at longer length scales, and simultaneously reduces accessible free volume through pore infiltration. Ionic content therefore governs matrix densification not by collapsing the backbone but by reshaping the free-volume landscape – an effect that underpins the mechanical and transport responses discussed in later sections.

2.1.3. Resolving the intermolecular interaction landscape. The structural analyses above establish that ILs densify the polymer matrix by infiltrating intrinsic voids while preserving global chain packing. This raises a key mechanistic question: does the IL behave merely as a confined guest, or does it actively engage in specific intermolecular interactions that reorganize the local environment? To address this, we quantified molecular-scale interactions using radial distribution functions (RDFs, $g(r)$) and neighbor-density ($\rho(r)$) analyses derived from MD simulations.

The total RDF profile (Fig. 6) reveals that most short-range bonded and non-bonded peaks remain invariant in position with increasing IL content, indicating that the underlying covalent framework of the polymer is preserved. For example, the H–C peak near 1.08 Å shows minimal change in location

 This journal is © The Royal Society of Chemistry 2026

Open Access Article. Published on 04 March 2026. Downloaded on 5/11/2026 10:44:53 PM.
This article is licensed under a Creative Commons Attribution-NonCommercial 3.0 Unported Licence.

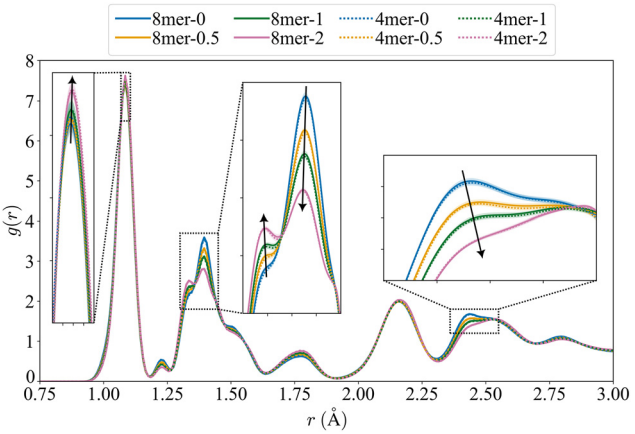

Fig. 6 Total radial distribution functions $g(r)$ with various ionic liquid concentrations. Black arrows denote peak shifting directions as ionic concentration increases.

and intensity. In contrast, intensity redistribution occurs between the adjacent C–C peaks at 1.34 and 1.41 Å – reflecting the introduction of IL-specific local environments. At larger distances (~2.5 Å), peak broadening becomes more evident as IL concentration increases, suggesting growing configurational heterogeneity driven by ionic screening and local relaxation from the IL.

Because RDFs are normalized by bulk density, changes in peak height can conflate coordination effects with densification. To isolate true coordination changes, we therefore evaluated the neighbor density, $\rho(r)$ (eqn (3)),

$$\rho(r) = 4\pi r^2 \rho_0 g(r) \quad (3)$$

which scales $g(r)$ by the bulk number density ρ_0 and spherical shell volume (Fig. 7 and 8). This analysis enables direct comparison across systems with differing compaction.

Polymer–polymer interactions, quantified through $\rho(r)$ for H_{chain}–N_{chain} and (Fig. 7 and S2(e)) and H_{chain}–O_{chain}

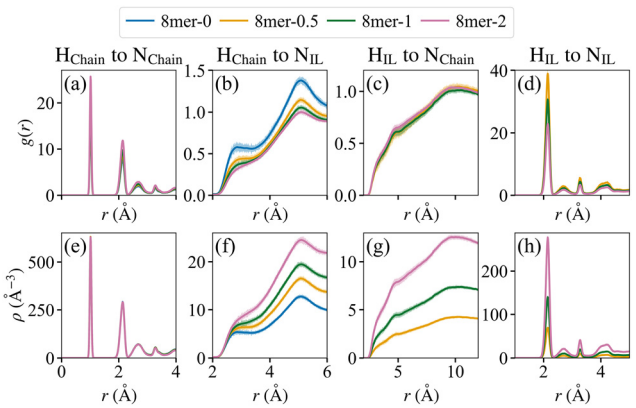

Fig. 7 (a)–(d) Radial distribution functions, $g(r)$, and (e)–(h) neighbor density, $\rho(r)$, for hydrogen, H, and nitrogen, N, interactions among (a) and (e) chain-to-chain, (b), (c), (f) and (g) chain-to-IL, and (d) and (h) IL-to-IL pairs for 8-mer systems. The corresponding analysis for 4-mers is provided in Fig. S2.

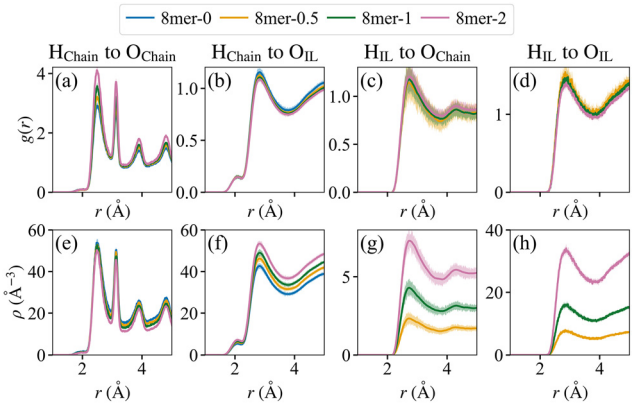

Fig. 8 (a)–(d) Radial distribution functions, $g(r)$, and (e)–(h) neighbor density, $\rho(r)$, for hydrogen, H, and oxygen, O, interactions among (a) and (e) chain-to-chain, (b), (c), (f) and (g) chain-to-IL, and (d) and (h) IL-to-IL pairs for 8-mer systems. The corresponding analysis for 4-mers is provided in Fig. S3.

(Fig. 8 and S3(e)), remain nearly unchanged across the IL concentration range, confirming that the polymer's internal cohesion is largely preserved even as the matrix densifies. In contrast, polymer–IL interactions increase systematically with IL loading. The most pronounced enhancements occur for H_{IL}–N_{chain} and H_{IL}–O_{chain} pairs (Fig. 7, 8, S2, and S3(g)), indicating strong hydrogen-bonding and ion-dipole interactions between imidazolium cations and polymer functional groups.

Coordination involving anion-centered sites shows more modest increases at short distances (Fig. 7, 8, S2, and S3(f)), consistent with saturation of available hydrogen-bond donors near the backbone. Meanwhile, IL–IL interactions strengthen steadily with increasing IL content, as evidenced by enhanced $\rho(r)$ for H_{cation}–N_{anion} and H_{cation}–O_{anion} pairs (Fig. 7, 8, S2, and S3(i)). These trends indicate the formation of increasingly coordinated ionic clusters with the polymer matrix.

The coexistence of strong cation–polymer interactions and growing IL–IL associations contributes to the broadened RDF features observed at intermediate distances and reflects a locally reorganized H-bonding environment. Crucially, the analysis demonstrates that the IL is not an inert filler. Instead, it actively restructures the local coordination landscape through specific, directional interactions while leaving the global polymer packing motif intact. These molecular-level associations underpin the densification and nanostructural disruption observed experimentally and provide a mechanistic foundation for the mechanical properties and transport behavior discussed in the following sections.

2.2. Thermomechanical and self-healing properties

The structural reorganization induced by IL incorporation directly reshapes the polymer's mechanical response and damage-recovery behavior. Because thermomechanical properties in ionene networks are governed by the balance between segmental mobility, supramolecular cohesion, and reversible ionic interactions, we next examined how ionic content modulates thermal stability, mechanical stiffness, and self-healing behavior across both experimental and simulation frameworks.

Open Access Article. Published on 04 March 2026. Downloaded on 5/11/2026 10:44:53 PM.
This article is licensed under a Creative Commons Attribution-NonCommercial 3.0 Unported Licence.

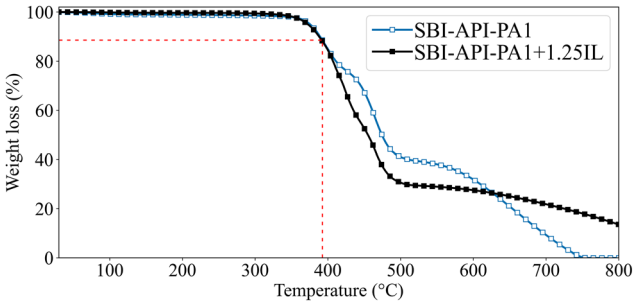

Fig. 9 TGA curves for SBI-TC-API-PA1 (open symbols) and the 1.25 eq IL composite (filled symbols). IL incorporation minimally reduces the onset of thermal degradation.

Table 1 Thermal degradation and glass transition temperatures of pristine SBI-TC-API-PA1 and the composite containing 1.25 eq of IL

Sample	$T_{10\%}$ [a] (°C)	$T_{50\%}$ [b] (°C)	T_g [c] (°C)
SBI-TC-API-PA1	390	475	100
SBI-TC-API-PA1 + 1.25IL	385	455	45

[a] Temperature at 10% weight loss (TGA). [b] Temperature at 50% weight loss (TGA). [c] Glass transition temperature (DSC).

2.2.1. Thermomechanical properties. Thermogravimetric analysis (TGA) confirms that the neat SBI-TC-API-PA1 ionene exhibits excellent thermal stability, with 10% and 50% mass losses not occurring until 390 °C and 475 °C, respectively (Fig. 9 and Table 1). Incorporation of 1.25 equivalents (eq) of IL produces only a modest decrease in these temperatures (to 385 °C and 455 °C), indicating that the rigid, aromatic-rich backbone confers substantial thermal robustness even in the presence of a mobile ionic component.

In contrast to the minimal effect on thermal degradation, IL incorporation has a pronounced impact on segmental dynamics as reflected in the glass transition temperature, T_g. Differential scanning calorimetry (DSC) reveals a dramatic decrease in T_g, from 100 °C in the neat polymer to 45 °C at 1.25 eq IL (Fig. 10). This shift directly reflects enhanced segmental mobility and reduced kinetic constraints, consistent with MD-derived reduction in FFV (Fig. 4c) and increased conformational relaxation observed at higher ionic content (Fig. 5).

Together, these results demonstrate that IL incorporation decouples thermal stability from segmental dynamics, lowering the kinetic barriers for rearrangement while preserving the polymer's intrinsic resistance to thermal degradation. IL molecules, therefore, act as dynamic plasticizers that lower the energy barrier for chain motion while maintaining the integrity of the covalent backbone.

2.2.2. Self-healing behaviors. The pronounced reduction in T_g with increasing IL content suggests that ionic incorporation should strongly accelerate damage recovery by enabling faster interdiffusion and re-association of polymer segments. This hypothesis is confirmed by direct experimental observation. As shown in Fig. 11, the neat polymer exhibits only partial crack closure after 16 h at 100 °C (its T_g). In contrast, the film containing 1.25 eq IL nearly fully restores its integrity within 1 h at 50 °C, just above its reduced T_g of 45 °C. This pronounced acceleration demonstrates that IL-enhanced mobility enables healing under substantially milder thermal conditions. To quantitatively assess how ionic content influences mechanical responses and recovery, we employed triaxial tensile simulations, which avoid directional artifacts associated with uniaxial loading and provide a more isotropic measure of network deformation (Fig. 12). All systems were strained at a

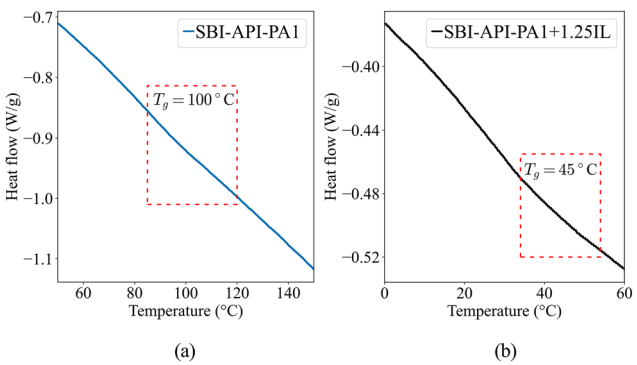

Fig. 10 DSC thermograms for (a) pristine SBI-TC-API-PA1 and (b) SBI-TC-API-PA1 with 1.25 eq IL. IL addition significantly lowers the glass transition temperature.

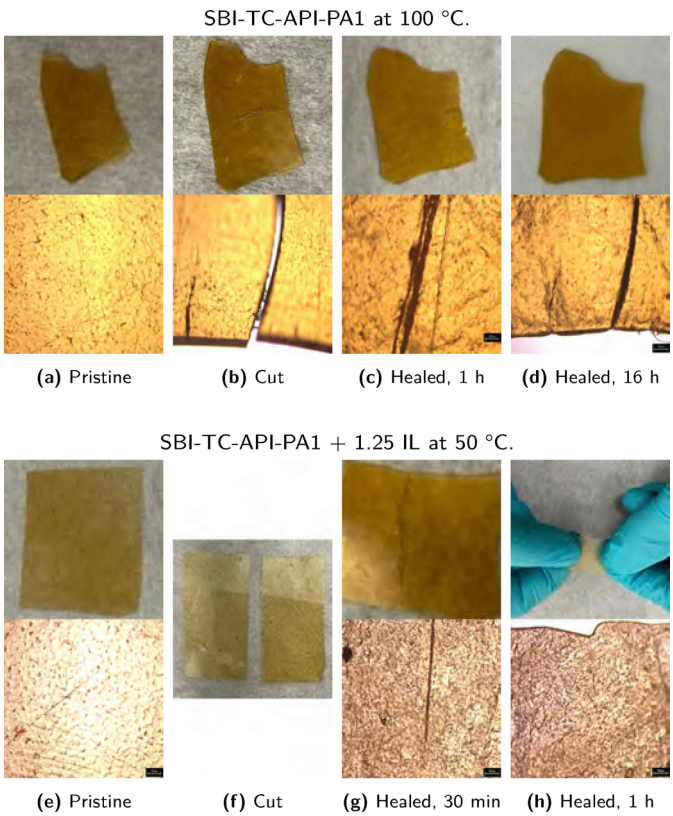

Fig. 11 Self-healing behavior of (a)–(d) neat SBI-TC-API-PA1 at 100 °C and (e)–(h) SBI-TC-API-PA1 with 1.25 eq IL at 50 °C. IL incorporation enables rapid crack closure near its reduced T_g.

This journal is © The Royal Society of Chemistry 2026

Open Access Article. Published on 04 March 2026. Downloaded on 5/11/2026 10:44:53 PM.
This article is licensed under a Creative Commons Attribution-NonCommercial 3.0 Unported Licence.

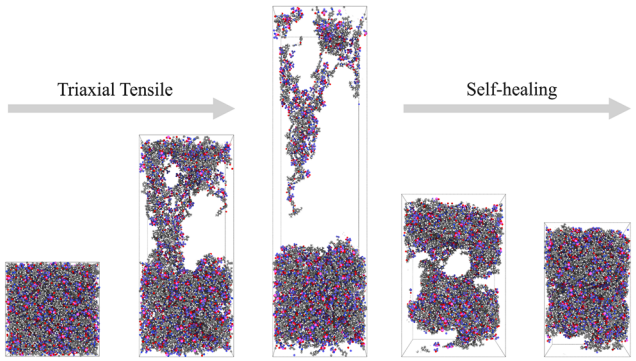

Fig. 12 Schematic of the triaxial tensile test illustrating deformation and subsequent self-healing behaviors.

rate of 10^{-6} fs^{-1} at 374 K to ensure comparable rubbery-state dynamics across compositions, independent of their differing T_g values.

The resulting stress–strain curves (Fig. 13) show that both Young's modulus and ultimate tensile strength (UTS) decrease monotonically with increasing IL concentration. This softening reflects systematic changes in the non-covalent interaction landscape under strain. As deformation proceeds, Poisson-driven lateral densification, which is normally responsible for strengthening short-range repulsions, becomes less effective, while chain–IL interactions weaken due to disruption of ionic coordination (Fig. 14). Together, these effects reduce efficient stress transfer across the network, yielding classical plasticization behavior consistent with the experimentally observed T_g depression and enhanced strain-induced energy dissipation.[39]

To bridge experimental and computational timescales and access nonequilibrium recovery processes, we performed high-temperature (600 K) post-fracture relaxation simulations (Fig. 15) to enable rapid network reorganization within nanoseconds. The elevated temperature accelerates molecular mobility by lowering kinetic barriers without causing bond scission or changing the fundamental interaction patterns of the network. Fitting strain–time profiles to exponential decay functions to extract characteristic relaxation times (τ) reveals a dramatic IL-induced acceleration of recovery dynamics. While these τ values are not intended for direct kinetic scaling to

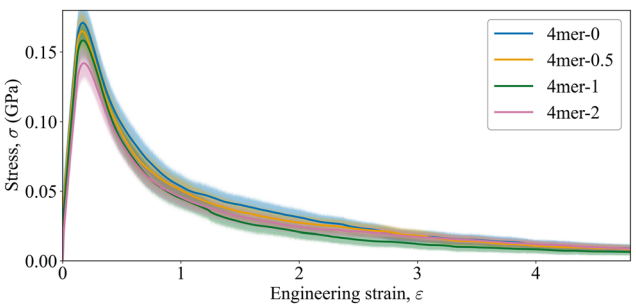

Fig. 13 Stress–strain responses from triaxial tensile tests on 4-mer systems with varying IL content. IL incorporation progressively softens the network and lowers both modulus and tensile strength. Shaded bands indicate the standard error of the mean.

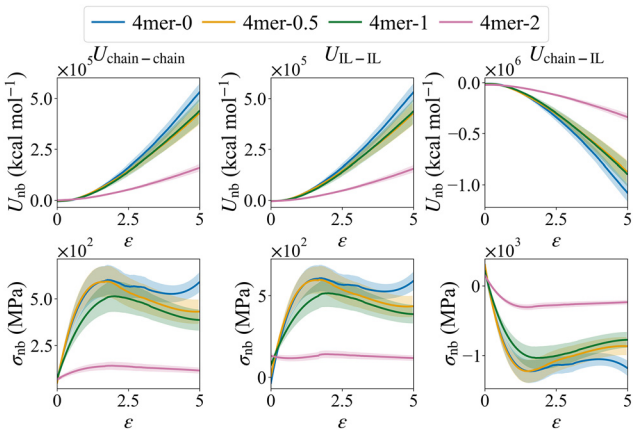

Fig. 14 Evolution of non-bonded (nb) potential energy (U_{nb}), and corresponding non-bonded stress contribution (σ_{nb}), during triaxial deformation, comparing chain–chain, IL–IL, and chain–IL interactions at different IL concentrations. Shaded bands represent the standard error of the mean.

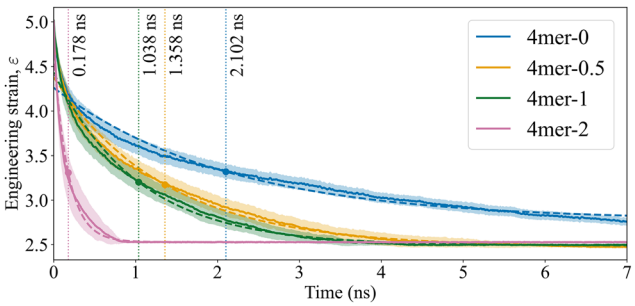

Fig. 15 Simulated strain–time relaxation profiles from post-fracture simulations at 600 K. Dashed vertical lines mark the healing relaxation time, τ, which is determined *via* exponential decay fits to the simulated data (represented by dashed and solid curves, respectively). IL-rich systems recover an order of magnitude faster than the pristine polymer.

macroscopic healing, they serve as a measure of how ionic content governs recovery dynamics. The pristine polymer relaxes slowly ($\tau \approx 2.10$ ns), whereas the IL-rich system recovers nearly an order of magnitude faster ($\tau \approx 0.18$ ns), consistent with enhanced dynamic freedom. Nonetheless, the pristine system retains significantly higher residual stress, reflecting incomplete structural reorganization. To quantify the extent of mechanical restoration, a second triaxial tensile test was applied to healed configurations. Because healing leaves residual deformation, engineering strain was re-zeroed at the onset of loading (Fig. 12). As shown in Fig. 16, both UTS and modulus decrease relative to pristine values after healing, indicating incomplete recovery of the original stiffness. Importantly, moderate IL incorporation substantially mitigates this deterioration. Healing efficiency, defined as the ratio of healed to pristine mechanical properties, η, exhibits a clear maximum near 0.5 eq IL (Fig. 17(b)). At this intermediate concentration, segmental mobility is sufficient to enable molecular rearrangement and interfacial reconnection, while interfacial cohesion remains strong enough to reestablish load-bearing pathways. Below this concentration, restricted mobility limits

Open Access Article. Published on 04 March 2026. Downloaded on 5/11/2026 10:44:53 PM. This article is licensed under a Creative Commons Attribution-NonCommercial 3.0 Unported Licence.

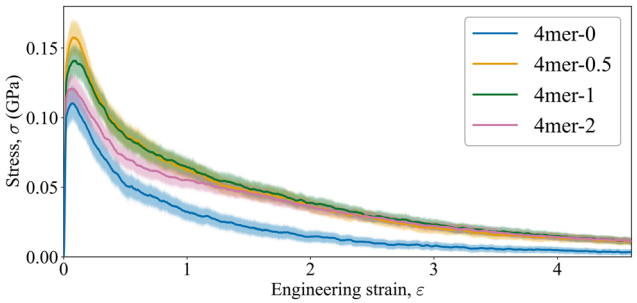

Fig. 16 Stress–strain responses of 4-mer polymer systems from the second triaxial tensile tests, highlighting ionic liquid concentration effects.

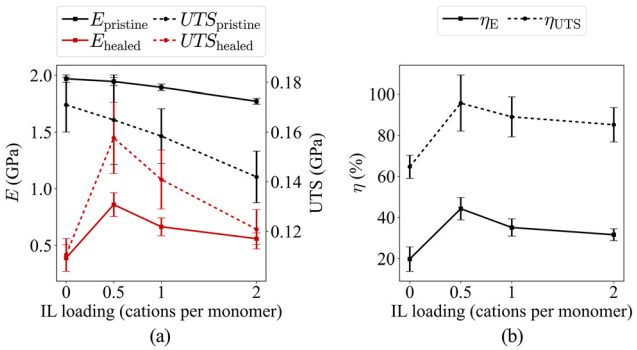

Fig. 17 Mechanical properties and healing performance of 4-mer systems. (a) Young's modulus (E, solid lines) and ultimate tensile strength (UTS, dashed lines) as a function of IL loading for pristine (black) and healed (red) states. (b) Healing efficiency (η) calculated from the recovery of the modulus (solid line, η from E) and the ultimate tensile strength (dashed line, η from UTS). The healing efficiency is defined as $\eta = (X_{healed}/X_{pristine}) \times 100\%$, where X represents either E or UTS; error bars represent the standard error of the mean.

reorganization; above it, excessive plasticization prevents full recovery of stiffness.

These results reveal a non-monotonic relationship between ionic content and healing performance. IL incorporation accelerates nonequilibrium relaxation and damage repair, but optimal mechanical recovery occurs only within an intermediate mobility window, where dynamic rearrangement and supramolecular cohesion are simultaneously preserved.

2.3. Gas transport and molecular interactions with CO_2

Gas transport in polymer membranes emerges from the coupled interplay between molecular-scale sorption, segmental mobility, and the connectivity of free-volume pathways. In ionene-based systems, this interplay is further modulated by ionic coordination and dynamic heterogeneity. Having established how ionic content restructures the polymer matrix (Section 2.1.) and governs nonequilibrium mechanical relaxation and healing (Section 2.5.), we now examine how these same interactions shape CO_2 transport behavior across molecular and macroscopic length scales.

2.3.1. Permeation and site-specific sorption. To evaluate transport behavior under experimentally relevant conditions, we characterized single-gas permeation through the SBI-TC-API-PA1 with 1.25 eq IL (the neat polymer was unable to withstand the pressure for gas transport due to its fragility), which forms uniform, mechanically robust films. Measurements conducted at 35 °C reveal a moderate yet well-balanced transport profile (Table 2). CO_2 permeability exceeds that of N_2 and CH_4, yielding ideal selectivities of $\alpha(CO_2/N_2)$ = 7.28 and $\alpha(CO_2/CH_4)$ = 5.23. These values indicate a sorption-dominated separation regime in which gas-matrix affinity plays a central role.

Table 2 Gas transport properties for SBI-TC-API-PA1-1.25IL

Permeability, P_i[a] (Barrer)				
H_2	N_2	O_2	CO_2	CH_4
4.53 ± 0.15	1.28 ± 0.17	2.14 ± 0.27	9.32 ± 0.13	1.78 ± 0.23
Ideal selectivity, $\alpha = P_i/P_j$				
CO_2/N_2	CO_2/O_2	CO_2/CH_4	CO_2/H_2	O_2/N_2
7.28	4.35	5.23	2.05	2.45

[a] Barrer = 10^{-10} cm^3 (STP) $cmcm^{-2}$ s^{-1} $cmHg^{-1}$.

The elevated CO_2 permeability is consistent with the presence of polar and ionic moieties within the polymer–IL framework, which transiently stabilize CO_2 without immobilizing it. In contrast, selectivities involving similarly sized, fast-diffusing gases (*e.g.*, CO_2/H_2, O_2/N_2) are lower, reflecting the increasing importance of mobility differences when size exclusion is weak. Together, these data indicate that transport in this system is governed not by large-scale pore connectivity alone, but by local interactions and dynamic accessibility of sorption sites.

To identify the molecular origins of these affinities, we performed density functional theory (DFT) calculations on representative polymers and IL fragments. Optimized CO_2 binding configurations (Fig. 18) show that CO_2 preferentially associates with sites of local charge and polarity. The strongest interactions occur with the $[Tf_2N]^-$ anion through dipolar interactions with sulfonyl oxygens, followed by imidazolium sites *via* polarized C–H and heteroatoms interactions. Amide groups provide moderate stabilization, while aromatic rings contribute only weak π-dispersion interactions. Computed binding energies (Fig. 19) fall within the physisorption regime (−23 to −39 kJ mol^{-1}), indicating reversible, transient association rather than permanent trapping. While these gas-phase values serve as a comparative metric rather than a direct prediction of condensed-phase thermodynamics, the noncovalent nature of the interaction is confirmed by structural analysis; CO_2 remains nearly linear in all optimized geometries, showing no significant bond elongation, angle distortion, or proton transfer.

These results establish that CO_2 transport is governed by selective, reversible sorption at polar and ionic sites embedded within a dynamically reorganizing matrix. Site-specific affinity enhances CO_2 uptake while preserving mobility, setting the stage for a transport response controlled by both solubility and dynamics.

2.3.2. Diffusivity analysis from ultrafast structural dynamics. While static sorption energetics identify preferred binding sites,

 This journal is © The Royal Society of Chemistry 2026

Open Access Article. Published on 04 March 2026. Downloaded on 5/11/2026 10:44:53 PM.
This article is licensed under a Creative Commons Attribution-NonCommercial 3.0 Unported Licence.

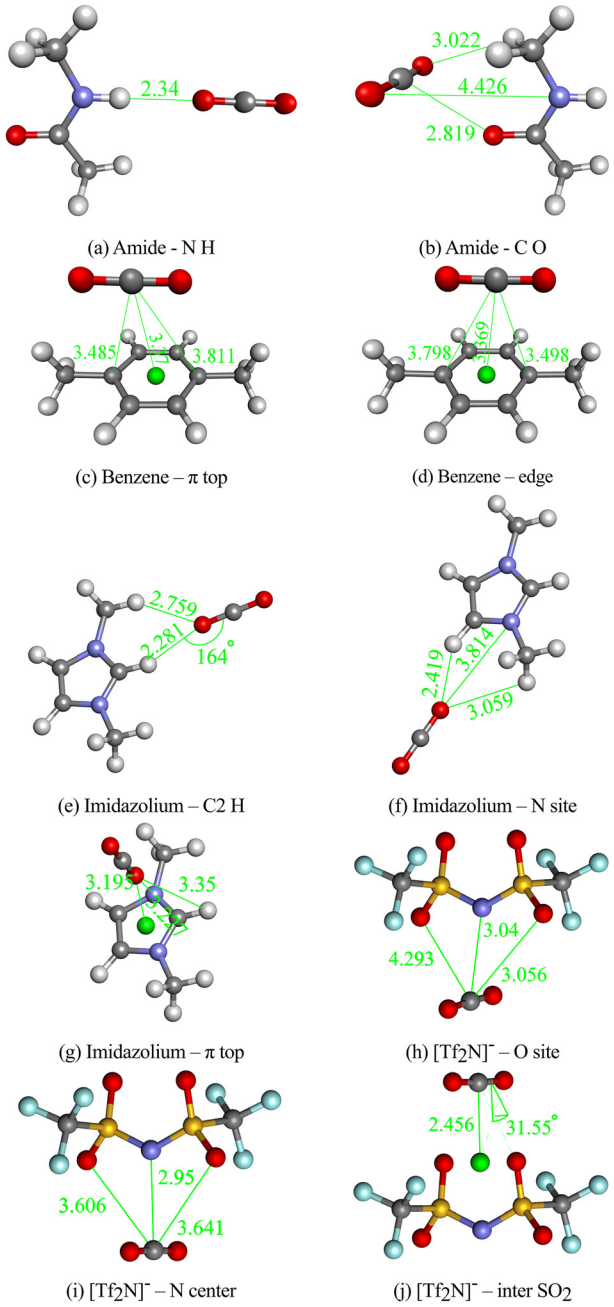

Fig. 18 DFT-optimized CO_2 binding configurations on representative polymer and IL fragments, illustrating local minimum energy configurations for various interaction sites: (a) and (b) amide nitrogen–hydrogen bond and carbonyl oxygen; (c) and (d) benzene π-top and edge-plane; (e)–(g) imidazolium C2–H, nitrogen heteroatom, and π-system; (h)–(j) $[Tf_2N]^-$ sulfonyl oxygen, central nitrogen, and inter-sulfonyl (SO_2) pocket. Green numbers denote intermolecular distances in Ångströms (Å) and binding angles in degrees (°). The green spheres within the aromatic and heterocyclic rings represent the ring centroids, while the green sphere between the sulfonyl groups in (j) represents the bisecting midpoint between two sulfonyl oxygens. Colored spheres identify atom types: carbon (grey), hydrogen (white), oxygen (red), nitrogen (blue), sulfur (yellow), and fluorine (light blue). Similar structures result from distinct starting orientations (see Fig. S4) converging to the same local stationary points.

macroscopic permeability also depends critically on how molecular mobility evolves within the polymer–IL matrix. To resolve dynamic contributions to transport, we analyzed mean-square displacements (MSD) of polymer segments, $[C_4mim]^+$ cations, and $[Tf_2N]^-$ anions (Fig. 20) across multiple time regimes with their corresponding power-law fitting parameters used to quantify these dynamical regimes summarized in Table 3.

For all species and IL concentrations, MSDs exhibit subdiffusive behavior ($\alpha < 1$), reflecting dynamic constraints imposed by polymer connectivity, ionic coordination, and restricted free volume. The prefactor A, which captures local vibrational and rattling motion, increases monotonically with IL loading, indicating enhanced short-range mobility due to plasticization and electrostatic screening. In contrast, the motional exponent α reveals a more complex, time-dependent response.

At short times (<0.3 ns), α is nearly independent of IL concentration for all species, consistent with the invariance of short-range structure observed in RDF (Fig. 6) and WAXS (Fig. 3a) analyses. At intermediate times (0.3–0.55 ns), pronounced differences emerge: polymer segments and cations exhibit strong caging at low and moderate IL loadings (4mer-0 to 4mer-1), while higher IL content reduces confinement and enables greater mobility. $[Tf_2N]^-$ anions show a monotonic increase in α with IL concentration, reflecting their increasing residence in IL-rich, less restrictive domains.

At long times (0.55–1 ns), α decreases with increasing IL concentration for all species, signaling the emergence of collective, correlated dynamics. Despite enhanced local motion, long-range transport becomes increasingly hindered by crowding and ionic clustering. This separation between fast local relaxation and suppressed long-range diffusion highlights the heterogeneous dynamics landscape created by ionic incorporation.

Because CO_2 interacts strongly with both polymer functional groups and anions, its mobility is expected to couple most closely to anion dynamics. Reduced anion caging at intermediate times enhances local CO_2 motion, while collective constraints at longer times limit macroscopic diffusion. CO_2 diffusion, therefore, reflects a balance between fast, short-range motion and increasingly correlated long-range dynamics. This dynamic competition reconciles the strong sorption affinity identified by DFT with the moderate permeability observed experimentally.

2.3.3. The solubility-diffusivity counterbalance. To quantify solubility contributions to permeability, we computed CO_2 solubility coefficients using Widom test-particle insertion. At 294 K, we implemented a sampling protocol of 2000 non-perturbative insertions every 50 timesteps, extending the production window to 20 000 steps to ensure the running average of the excess chemical potential reached a stable, converged plateau across independent configurations. A non-interacting CO_2 probe was placed at random positions in the equilibrated cell, and the corresponding interaction-energy change ΔU was sampled to compute the excess chemical potential μ_{ex} (eqn (4))

$$\mu_{ex} = -k_B T \ln\langle \exp[-\Delta U/(k_B T)]\rangle, \quad (4)$$

Open Access Article. Published on 04 March 2026. Downloaded on 5/11/2026 10:44:53 PM.
This article is licensed under a Creative Commons Attribution-NonCommercial 3.0 Unported Licence.

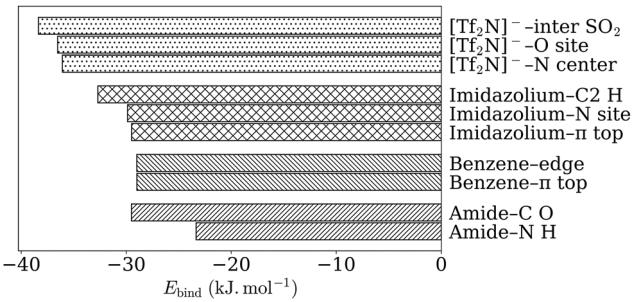

Fig. 19 CO_2 binding energies computed at the WB97X-D/def2-TZVPD level for representative functional sites, showing stronger interactions with ionic and polar regions.

averaged over independent trajectories to ensure robust statistics. The Henry-law solubility coefficient K_s is then

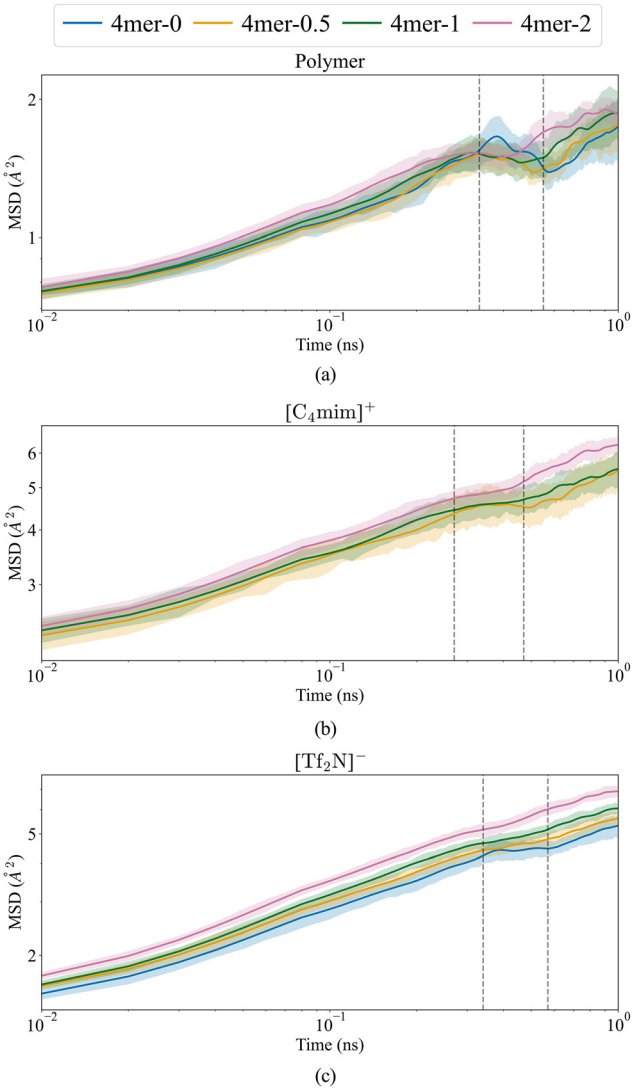

Fig. 20 MSD plotted on log–log scales for (a) 4-mer polymer chains, (b) $[C_4mim]^+$ cations, and (c) $[Tf_2N]^-$ anions as a function of IL concentration; shaded regions represent SD. Dashed vertical lines mark the window boundaries used in the piecewise power-law regression of the MSD. The corresponding MSD results for 8-mers are provided in Fig. S5.

Table 3 Power-law exponents A and α from MSD fits, $MSD(t) = At^{\alpha}$, for the polymer, $[C_4mim]^+$ cation, and $[Tf_2N]^-$ anion in 4-mer systems. Time windows are listed in the table. The corresponding 8-mer fit parameters are reported in Table S6

	Window 1		Window 2		Window 3	
	A	α	A	α	A	α
Polymer	(0.01–0.33)		(0.33–0.55)		(0.55–1.0) ns	
4mer-0	1.88	0.22	—	0.00[a]	1.75	0.43
4mer-0.5	1.87	0.22	—	0.00[a]	1.79	0.39
4mer-1	1.95	0.23	—	0.00[a]	1.90	0.36
4mer-2	2.00	0.22	1.87	0.22	1.92	0.20

	Window 1		Window 2		Window 3	
	A	α	A	α	A	α
Cation	(0.01–0.27)		(0.27–0.47)		(0.47–1.0) ns	
4mer-0	—	—	—	—	—	—
4mer-0.5	5.60	0.20	4.79	0.06	5.47	0.28
4mer-1	5.82	0.21	4.99	0.08	5.51	0.21
4mer-2	6.26	0.22	5.64	0.14	6.37	0.26

	Window 1		Window 2		Window 3	
	A	α	A	α	A	α
Anion	(0.01–0.34)		(0.34–0.57)		(0.57–1.0) ns	
4mer-0	5.86	0.31	4.70	0.08	5.36	0.34
4mer-0.5	6.21	0.31	5.21	0.16	5.66	0.29
4mer-1	6.75	0.33	5.73	0.20	6.12	0.28
4mer-2	7.58	0.34	7.16	0.32	7.00	0.26

[a] Fits in this interval are noise-dominated and consistent with a plateau ($\alpha \approx 0$); small negative values may arise from MSD fluctuations.

given by (eqn (5))

$$K_s = \frac{c}{p} = \frac{\langle \exp[-\Delta U/(k_B T)] \rangle}{RT}, \quad (5)$$

where K_s reflects the infinite-dilution solubility of CO_2 in the matrix, k_B and R are the Boltzmann and gas constants, respectively, and T is temperature.

The resulting solubility coefficients (Fig. 21) exhibit a non-monotonic dependence on ionic content. At low IL loadings, solubility decreases due to matrix densification and reduced cavity accessibility, consistent with FFV and SAXS results. At intermediate IL concentrations, solubility partially recovers as additional polar and ionic sites enhance transient CO_2 binding. At higher IL loadings, solubility decreases again as free-volume elements become oversaturated and increasingly constrained.

Within the solution–diffusion framework, permeability reflects the product of solubility and diffusivity (eqn (1)). Here, these contributions evolve in opposing directions: densification reduces solubility (K_s), while enhanced ionic mobility promotes diffusion (D). MSD-derived trends indicate that the permeability could remain stable, or even increase at intermediate IL contents where mobility gains outweigh solubility losses. Although explicit CO_2 self-diffusion coefficients were not computed here, the combined solubility estimates (Widom insertion) and the observed changes in ionic/segmental dynamics suggest a plausible solubility–diffusivity counterbalance

This journal is © The Royal Society of Chemistry 2026

Open Access Article. Published on 04 March 2026. Downloaded on 5/11/2026 10:44:53 PM. This article is licensed under a Creative Commons Attribution-NonCommercial 3.0 Unported Licence.

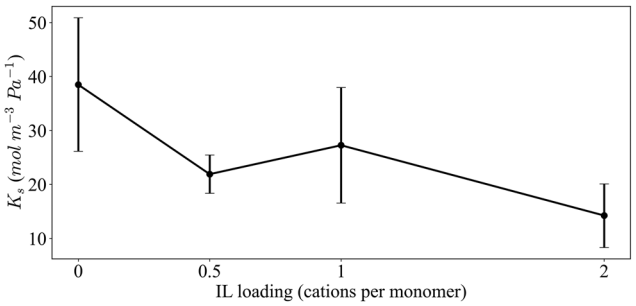

Fig. 21 CO_2 solubility of 4-mers from Widom test-molecule insertions as a function of ionic content, showing the balance between densification and electrostatic interactions; error bars represent the standard error of the mean.

underlying the measured permeability trends. We emphasize that this interpretation should be viewed as a testable prediction rather than a direct experimental demonstration. Direct validation will require independent experimental determination of CO_2 sorption and/or diffusion (*e.g.*, sorption isotherms and time-lag analysis) across multiple IL loadings.

3. Conclusion

In summary, ionic content provides a single, powerful control parameter for tuning the structure, dynamics, and function of SBI-based PA-ionene networks. By integrating intrinsic microporosity with imidazolium-driven reversible interactions, the material undergoes hierarchical reorganization: IL molecules fill intrinsic micropores, extend chain conformations, and restructure local coordination environments while preserving global packing. These changes selectively enhance segmental mobility, lowering T_g, and enabling rapid self-healing under mild conditions. At intermediate IL loadings, mobility and cohesion are optimally balanced, producing the highest healing efficiency.

Gas transport reflects the same coupled physics. CO_2 sorption is governed by polar and ionic sites, while diffusion is shaped by heterogeneous ionic dynamics and free-volume redistribution. The resulting solubility-diffusivity counterbalance links transport performance directly to the same ionic interactions that drive mechanical recovery.

Together, these results establish a generalizable design principle: functional performance in adaptive microporous polymers emerges from tuning the interplay between mobility and cohesion through controlled ionic interactions. This structure–dynamics–transport framework provides a blueprint for designing next-generation soft-matter systems that combine mechanical resilience, reconfigurability, and selective transport.

4. Methodology

4.1. Materials synthesis and characterization

4.1.1. Materials. Triethylamine (TEA), 4-(chloromethyl)-benzoyl chloride (98%) were purchased from BeanTown Chemical. Lithium bistriflimide ($LiTf_2N$) (99%) was purchased from IoLiTec. IL $[C_4mim][Tf_2N]$ were previously synthesized by Bara's group.[29,40–43] All other reagents and solvents were purchased from commercial suppliers as analytical grade and used without further purification.

4.1.2. Synthesis of the dihalogenated monomer. In a 250 mL round-bottom flask, 3.0 g (9.3 mmol) of diamine **4** was dissolved in 50 mL of dry dichloromethane (DCM) under an inert atmosphere. The solution was cooled to 0 °C in an ice bath, and 2.5 equiv. of triethylamine (TEA, 23.3 mmol, 3.25 mL) were added dropwise with stirring. After 10 min, 2.2 equiv. of 4-(chloromethyl)benzoyl chloride (4.20 g, 20.5 mmol) were added slowly while maintaining the temperature at 0 °C. The reaction was stirred at room temperature for 12 h under a N_2 atmosphere. The white solid obtained was filtered, washed with DCM, and dried at 80 °C for 12 h.

The successful preparation of monomer **5** was confirmed by its ^{1}H NMR spectrum (Fig. 22). The aliphatic resonances at 4.85 and 4.82 ppm (H1), 2.40–2.20 ppm (H3), and 1.42–1.33 ppm (H4, 5) appeared in the expected regions, while the aromatic signals displayed their characteristic multiplicities. The amide protons at 10.24 and 10.12 ppm and the systematic doubling of all peaks reflected the chemical nonequivalence of protons within the isomeric mixture.

4.1.3. Synthesis of polymer SBI-TC-API-PA1. In a 50 mL heavy-walled pressure vessel with a Teflon screw cap, 2.0 g (3.19 mmol) of the dihalogenated monomer was dissolved in 15 mL of dry *N*-methyl-2-pyrrolidone (NMP). One equivalent (1.20 g, 3.19 mmol) of TC-API was added under stirring, and the reaction mixture was heated at 180 °C for 24 h under continuous stirring. After cooling to room temperature, the supernatant NMP was decanted carefully, and the solid polymer was washed with fresh NMP (3 × 10 mL) to remove unreacted monomers and low-molecular-weight oligomers. The polymer was then dissolved in 50 mL of deionized water, and a solution of 10 equiv. of $LiTf_2N$ in 50 mL of H_2O was added dropwise while stirring. As the anion exchange proceeded, the polymer precipitated from the aqueous solution. The solid was collected by filtration, washed thoroughly with DI water (2 × 50 mL), and dried under vacuum at 60 °C overnight.

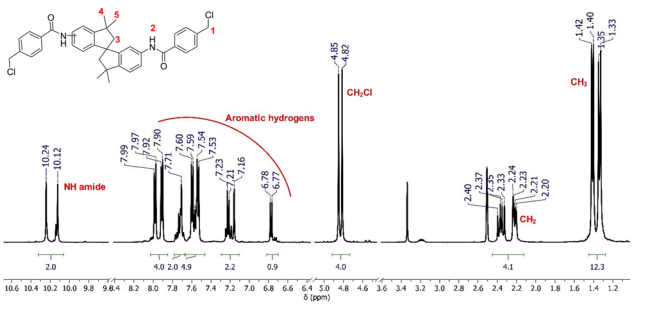

Fig. 22 Dihalogenated monomer **5**: yield: 92%. ^{1}H NMR (DMSO-d_6, δ, ppm) spectrum: 10.24, 10.12 (s, 2H, NH amide, H2); 7.99–6.77 (m, 14H, Ar–H); 4.85, 4.82 (s, 4H, CH_2 Cl, H1); 2.40–2.20 (m, 4H, CH_2, H3); 1.42–1.33 (s, 12H, CH_3, H4,5).

Open Access Article. Published on 04 March 2026. Downloaded on 5/11/2026 10:44:53 PM. This article is licensed under a Creative Commons Attribution-NonCommercial 3.0 Unported Licence.

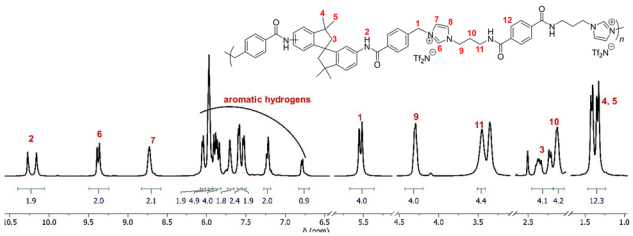

Fig. 23 SBI-TC-API-PA1: ^{1}H NMR (DMSO-d_6, δ, ppm) spectrum: 10.27, 10.16 (s, 2H, NH amide, H2); 9.39, 9.36 (s, 2H, H6); 8.72 (s, 2H, H7); 8.06–6.78 (m, 20H, aromatic hydrogens); 5.55, 5.52 (s, 4H, H1); 4.29 (s, 4H, H9); 3.45 (s, 4H, H11); 2.24–2.21 (m, 4H, H3); 2.13 (s, 4H, H10); 1.43–1.32 (s, 12H, H4,5).

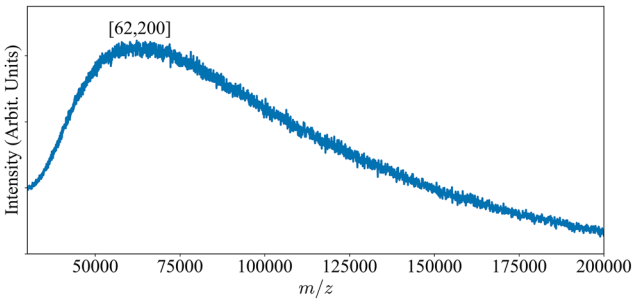

Fig. 24 MALDI-TOF curves for SBI-TC-API-PA1.

The ^{1}H NMR spectrum of SBI-TC-API-PA1 (Fig. 23) showed well-resolved aromatic resonances from the polymer backbone. A pronounced downfield shift of the imidazolium H6 proton confirmed successful quaternization. In the aliphatic region, peaks near 5.5 ppm (H1) were consistent with methylene groups linking the quaternary centers, while the amide protons (9.5–10.5 ppm) remained in a similar region as in monomer **5**, as expected.

4.1.4. Film preparation. Dense films were prepared using a 10 wt% solution of each polymer in DMF by the solution-casting method, involving an initial solvent evaporation at 50 °C followed by gradual oven heating from 50 °C to 120 °C over 5 days. Each solution was filtered through a 3.1 μm fiberglass Synta® syringe filter and poured into a circular Teflon® Petri dish placed on a level hot plate. The solvent was evaporated at 50 °C for 48 h, followed by gradual heating to 120 °C over 5 days.

The polymer's molecular weight was assessed by MALDI-TOF MS (Fig. 24), which revealed a number-average molecular weight (M_n) of 62.2 kDa (the IL [C_4mim][Tf_2N] was incorporated before filtration at loadings calculated relative to the polymer repeat unit mass). Although moderate in magnitude, this molecular weight was sufficient to yield robust, self-supporting films. We attribute the favorable mechanical behavior to the high aromatic content of the backbone, which promotes strong interchain π–π interactions. These interactions enhance rigidity and render the polymer morphology sensitive to changes in molecular packing.

4.1.5. Instrumentation. ^{1}H NMR spectra were recorded on a BRUKER AV500 (500 MHz) using DMSO-d_6 as solvent with TMS as an internal standard. MALDI-TOF MS measurements were conducted on a Bruker Ultraflex instrument using DCTB as the matrix (5 mg mL^{-1} in DMF). Thermal analyses were performed on a TA Instruments DSC Q2000 and a PerkinElmer TGA7 under N_2 atmosphere.

4.1.6. Small-angle X-ray scattering (SAXS) measurements. SAXS measurements were carried out using a Xenocs Xeuss 3.0 instrument equipped with a D2+ MetalJet X-ray source operating at 9.2 keV (Ga Kα radiation, λ = 1.3414 Å). Sample films were mounted on a sample holder and aligned perpendicular to the incident X-ray beam in transmission geometry. The scattered X-rays were recorded using a two-dimensional (2D) Dectris Eiger 2R 4M hybrid photon-counting detector with a pixel size of 75 × 75 μm^2. The collected 2D SAXS patterns were circularly averaged and placed on an absolute intensity scale (cm^{-1}) using the known direct beam intensity. The sample-to-detector distances were calibrated to 370 mm for SAXS using the lanthanum hexaboride (LaB_6) standard. These calibrated distances were used for q calibration, where the magnitude of the scattering vector is defined as $q = 4\pi \sin\theta/\lambda$, with θ being half of the scattering angle. The exposure times were 600 s for SAXS measurements.

4.1.7. Wide-angle X-ray scattering (WAXS) measurements. WAXS patterns were collected on a Bruker D8 Discover diffractometer equipped with a general area detector diffraction system and Co Kα radiation (λ_{Co} = 1.590 Å). Scans were performed in reflection mode over a 2θ range of 10–60° with a step size of 0.02° and a counting time of 1 s per step. The d-spacings (d values) were calculated from the peak positions (q_0) using the relation $d = 2\pi/q_0$.

4.1.8. Gas permeation measurements. Pure-gas permeability coefficients were measured at 35 °C using a constant-volume, variable-pressure permeation cell. The downstream pressure was maintained at 10^{-2} mbar, while the upstream feed pressure was 2 bar. The gases used were H_2, O_2, N_2, CO_2, and CH_4 with purities greater than 99.95%. Film thicknesses were measured with a digital micrometer (±1 μm).

4.1.9. Mechanical and self-healing tests. Mechanical properties were evaluated on dense polymer films (approximately 5 mm × 20 mm) using a uniaxial tensile testing setup at a strain rate of 10^{-3} s^{-1}. Healing tests were conducted by cutting the films, bringing the edges into contact, and thermally treating at 50 °C for 1 h prior to retesting. The healing efficiency was calculated using the ratio of the healed property to the pristine property, $\eta = (P_{healed}/P_{pristine}) \times 100\%$. Representative stress–strain curves and optical micrographs before and after healing are shown in Fig. 11.

4.2. Computational methods

4.2.1. Atomistic molecular dynamics simulations. All-atom molecular dynamics simulations were performed using the LAMMPS package.[44] The molecular system was constructed from monomer units and parameterized using the all-atom optimized potentials for liquid simulations (OPLS-AA) force field[45] generated *via* LigParGen.[46] Atomic charges and bonded

 This journal is © The Royal Society of Chemistry 2026

Open Access Article. Published on 04 March 2026. Downloaded on 5/11/2026 10:44:53 PM. This article is licensed under a Creative Commons Attribution-NonCommercial 3.0 Unported Licence.

parameters were assigned automatically, without further modification. No charge scaling (*e.g.*, the commonly used 0.8 factor) was applied. Although reduced-charge schemes are often used in simulations of neat ionic liquids, unscaled OPLS-AA charges were retained here to preserve the chemically accurate electrostatics of the imidazolium-containing PA-ionene and the IL species, and to maintain a consistent and physically justified charge distribution across all components of the polymer–IL network. A total of 144 monomers were polymerized into chains containing either four (4-mer) or eight (8-mer), repeating units to investigate the influence of chain length on macromolecular behavior. To evaluate the effect of IL loading, four concentrations of $[C_4mim]^+[Tf_2N]^-$ (Fig. 1c) were incorporated into the system, enabling analysis of IL content on transport and mechanical properties. All-atom MD simulations were performed using LAMMPS,[44] employing periodic boundary conditions to mimic bulk behavior. Simulation processes and parameters used are presented in Section S1 of the SI.

Conflicts of interest

There are no conflicts to declare.

Data availability

The data supporting this article have been included as part of the supplementary information (SI), including all simulation details and force-field parameters, additional structural analyses for 4-mer systems, CO_2 binding configurations, and MSD of 8-mer systems. See DOI: https://doi.org/10.1039/d6sm00105j.

Acknowledgements

F. S., S. R., A. T. C., P. S. S., J. E. B., and J. A. M. acknowledge the support of the U.S. Department of Energy (DE- SC0023473). J. A. M. acknowledges the support of the National Science Foundation (NSF 2132055). SAXS measurements were performed under the user program (CNMS2023-A-01754) at the Center for Nanophase Materials Sciences (CNMS), a U.S. Department of Energy Office of Science User Facility operated by Oak Ridge National Laboratory. This research also utilized resources of the Neutron Scattering Division (NSD), which is also a U.S. Department of Energy Office of Science User Facility operated by Oak Ridge National Laboratory. All calculations in this work were performed at the Vermont Advanced Computing Center at the University of Vermont.

References

1 J. Rogelj, M. Den Elzen, N. Höhne, T. Fransen, H. Fekete, H. Winkler, R. Schaeffer, F. Sha, K. Riahi and M. Meinshausen, *Nature*, 2016, **534**, 631–639.
2 R. W. Baker and B. T. Low, *Macromolecules*, 2014, **47**, 6999–7013.
3 L. M. Robeson, *J. Membr. Sci.*, 1991, **62**, 165–185.
4 L. M. Robeson, *J. Membr. Sci.*, 2008, **320**, 390–400.
5 N. B. McKeown and P. M. Budd, *Macromolecules*, 2010, **43**, 5163–5176.
6 P. M. Budd and N. B. McKeown, *Polym. Chem.*, 2010, **1**, 63–68.
7 A. Wang, M. Zhao, Y. Weng and C. Zhang, *J. Membr. Sci.*, 2025, 124172.
8 B. Comesaña-Gándara, J. Chen, C. G. Bezzu, M. Carta, I. Rose, M.-C. Ferrari, E. Esposito, A. Fuoco, J. C. Jansen and N. B. McKeown, *Energy Environ. Sci.*, 2019, **12**, 2733–2740.
9 I. Kammakakam, K. E. O'Harra, J. E. Bara and E. M. Jackson, *Macromolecules*, 2022, **55**, 4790–4802.
10 A. G. McDermott, P. M. Budd, N. B. McKeown, C. M. Colina and J. Runt, *J. Mater. Chem. A*, 2014, **2**, 11742–11752.
11 C. Geng, Y. Sun, Z. Zhang, Z. Qiao and C. Zhong, *ACS Sustainable Chem. Eng.*, 2022, **10**, 3643–3650.
12 S. R. White, N. R. Sottos, P. H. Geubelle, J. S. Moore, M. R. Kessler, S. R. Sriram, E. N. Brown and S. Viswanathan, *Nature*, 2001, **409**, 794–797.
13 S. R. White, J. Moore, N. Sottos, B. Krull, W. Santa Cruz and R. Gergely, *Science*, 2014, **344**, 620–623.
14 J. F. Patrick, M. J. Robb, N. R. Sottos, J. S. Moore and S. R. White, *Nature*, 2016, **540**, 363–370.
15 D. Grigoriev, E. Shchukina and D. G. Shchukin, *Adv. Mater. Interfaces*, 2017, **4**, 1600318.
16 P. A. Pratama, M. Sharifi, A. M. Peterson and G. R. Palmese, *ACS Appl. Mater. Interfaces*, 2013, **5**, 12425–12431.
17 B. Li, P.-F. Cao, T. Saito and A. P. Sokolov, *Chem. Rev.*, 2022, **123**, 701–735.
18 T.-P. Huynh, P. Sonar and H. Haick, *Adv. Mater.*, 2017, **29**, 1604973.
19 C.-H. Huang and Y.-L. Liu, *RSC Adv.*, 2017, **7**, 38360–38366.
20 X. He, X. Sun, H. Meng, S. Deng, T. He, H. Zang and D. Wei, *J. Mater. Sci.*, 2021, **56**, 10231–10248.
21 L. R. Hart, J. L. Harries, B. W. Greenland, H. M. Colquhoun and W. Hayes, *Polym. Chem.*, 2013, **4**, 4860–4870.
22 F. Herbst, S. Seiffert and W. H. Binder, *Polym. Chem.*, 2012, **3**, 3084–3092.
23 R. Zhang, T. Yan, B.-D. Lechner, K. Schroter, Y. Liang, B. Li, F. Furtado, P. Sun and K. Saalwachter, *Macromolecules*, 2013, **46**, 1841–1850.
24 W. Zhang, H. Jiang, Z. Chang, W. Wu, G. Wu, R. Wu and J. Li, *J. Mater. Sci.*, 2020, **55**, 13543–13558.
25 S. Kupfer, L. Zedler, J. Guthmuller, S. Bode, M. D. Hager, U. S. Schubert, J. Popp, S. Gräfe and B. Dietzek, *Phys. Chem. Chem. Phys.*, 2014, **16**, 12422–12432.
26 P. Guo, H. Zhang, X. Liu and J. Sun, *ACS Appl. Mater. Interfaces*, 2018, **10**, 2105–2113.
27 X. He, G. Liu, Y. Zhang, G. Li and Y. Niu, *Macromolecules*, 2025, **58**, 2276–2288.
28 L. Gao, W. Jiang, X. Zhang, Y. Sun, K. Chen, W. Li, H. Xie and J. Liu, *Chem. Eng. J.*, 2024, **479**, 147822.
29 K. O'Harra, N. Sadaba, M. Irigoyen, F. Ruipérez, R. Aguirresarobe, H. Sardon and J. Bara, *ACS Appl. Polym. Mater.*, 2020, **2**, 4352–4359.

Open Access Article. Published on 04 March 2026. Downloaded on 5/11/2026 10:44:53 PM.
This article is licensed under a Creative Commons Attribution-NonCommercial 3.0 Unported Licence.

30 I. Kammakakam, K. E. O'Harra, G. P. Dennis, E. M. Jackson and J. E. Bara, *Polym. Int.*, 2019, **68**, 1123–1129.
31 O. Bertran, C. Saldas, D. D. Daz and C. Alemán, *Polymer*, 2020, **211**, 123072.
32 T. Walker, V.-Q. Vuong, S. Irle and J. Ma, *J. Comput. Chem.*, 2025, **46**, e70064.
33 K. E. O'harra, I. Kammakakam, D. M. Noll, E. M. Turflinger, G. P. Dennis, E. M. Jackson and J. E. Bara, *Membranes*, 2020, **10**, 51.
34 J. L. Shamshina and P. Berton, *Int. J. Mol. Sci.*, 2024, **25**, 1720.
35 J. S. Lee, A. Hocken and M. D. Green, *Mol. Syst. Des. Eng.*, 2021, **6**, 334–354.
36 Y. Miwa, J. Kurachi, Y. Kohbara and S. Kutsumizu, *Commun. Chem.*, 2018, **1**, 5.
37 M. Carta, R. Malpass-Evans, M. Croad, Y. Rogan, J. C. Jansen, P. Bernardo, F. Bazzarelli and N. B. McKeown, *Science*, 2013, **339**, 303–307.
38 A. Thran, H. Kroll and R. F. T. Steudel, *J. Polym. Sci., Part B: Polym. Phys.*, 1999, **37**, 3344–3358.
39 Y. E. A. Zhao, *Soft Matter*, 2022, **18**, 4472–4482.
40 K. E. O'Harra, G. M. Timmermann, J. E. Bara and K. M. Miller, *ACS Appl. Polym. Mater.*, 2021, **3**, 1995–2004.
41 S. Ravula, K. W. Wise, P. S. Shinde and J. E. Bara, *Macromolecules*, 2023, **56**, 6126–6141.
42 J. E. Bara, C. J. Gabriel, S. Lessmann, T. K. Carlisle, A. Finotello, D. L. Gin and R. D. Noble, *Ind. Eng. Chem. Res.*, 2007, **46**, 5380–5386.
43 D. Camper, J. E. Bara, D. L. Gin and R. D. Noble, *Ind. Eng. Chem. Res.*, 2008, **47**, 8496–8498.
44 S. Plimpton, *J. Comput. Phys.*, 1995, **117**, 1–19.
45 M. J. Robertson, J. Tirado-Rives and W. L. Jorgensen, *J. Chem. Theory Comput.*, 2015, **11**, 3499–3509.
46 L. S. Dodda, I. Cabeza de Vaca, J. Tirado-Rives and W. L. Jorgensen, *J. Comput. Chem.*, 2017, **38**, 1635–1641.

 This journal is © The Royal Society of Chemistry 2026